electronics

MDPI

Article

CNN-Based Vehicle Target Recognition with Residual Compensation for Circular SAR Imaging

Rongchun Hu [1,2,3], Zhenming Peng [1,2,*], Juan Ma [4] and Wei Li [1,2]

1 School of Information and Communication Engineering, University of Electronic Science and Technology of China, Chengdu 611731, China; hrc@swust.edu.cn (R.H.); liw@tsinghua.edu.cn (W.L.)
2 Laboratory of Imaging Detection and Intelligent Perception, University of Electronic Science and Technology of China, Chengdu 610054, China
3 School of Information Engineering, Southwest University of Science and Technology, Mianyang 621010, China
4 School of Science, Southwest University of Science and Technology, Mianyang 621010, China; majuan@swust.edu.cn
* Correspondence: zmpeng@uestc.edu.cn; Tel.: +86-28-8320-8819

Received: 11 February 2020; Accepted: 24 March 2020; Published: 26 March 2020



Abstract: The contour thinning algorithm is an imaging algorithm for circular synthetic aperture radar (SAR) that can obtain clear target contours and has been successfully used for circular SAR (CSAR) target recognition. However, the contour thinning imaging algorithm loses some details when thinning the contour, which needs to be improved. This paper presents an improved contour thinning imaging algorithm based on residual compensation. In this algorithm, the residual image is obtained by subtracting the contour thinning image from the traditional backprojection image. Then, the compensation information is extracted from the residual image by repeatedly using the gravitation-based speckle reduction algorithm. Finally, the extracted compensation image is superimposed on the contour thinning image to obtain a compensated contour thinning image. The proposed algorithm is demonstrated on the Gotcha dataset. The convolutional neural network (CNN) is used to recognize the target image. The experimental results show that the image after compensation has a higher target recognition accuracy than the image before compensation.

Keywords: circular SAR; vehicle target recognition; contour thinning; residual compensation; convolutional neural network

1. Introduction

Because of its all-day, all-weather imaging capability, synthetic aperture radar (SAR) has been widely used in military and civilian applications in recent years. There are different types of SAR depending on their mode of detection. One of the detection methods of SAR is to span a large azimuth in the process of data acquisition, which is called wide-angle SAR (WSAR). If the radar always shines on the same ground when detecting, and the azimuth turned around is large enough to make the radar's flight track a circle, it is called circular SAR (CSAR). CSAR is a special case of WSAR. Research based on SAR and CSAR includes time-frequency analysis, 2D/3D imaging, digital elevation model (DEM), target detection and recognition, etc. [1–11].

Research into CSAR began in the early 1990s [12–14]. Soumekh first proposed the imaging mode and echo signal time-domain model of CSAR in 1996, and also proposed the CSAR imaging algorithm based on wavefront reconstruction [15]. Subsequently, more and more research has been carried out on CSAR. Many of the datasets used in these studies are from the Air Force Research Laboratory (AFRL). AFRL has released several experimental and simulation datasets for WSAR and CSAR, as well as challenging related problems [16–19]. In addition to the datasets released by AFRL, some researchers

and organizations have conducted experiments on CSAR [20,21]. In the research on CSAR, imaging is an important research area. Imaging algorithms for CSAR include algorithms based on backprojection, wavefront reconstruction, compressed sensing, and other algorithms. Many researchers have proposed different imaging algorithms. Hong and Lin et al. carried out a series of studies on the imaging of CSAR and achieved good results [22–28]. Kou et al. carried out a series of studies on geosynchronous CSAR imaging, and analyzed the effects of orbit error, L-band of troposphere and high sidelobe on imaging [29–31]. Yuan et al. proposed a method for reconstructing SAR images that is built upon the backprojection algorithm using multiple sub-aperture images to attain both greater processing efficiency and improved image quality [32]. Chen et al. proposed a processing strategy for the 3D reconstruction of vehicles, which only needs the single-pass single-polarization CSAR data [33]. Among these imaging algorithms, the backprojection algorithm is the most widely used imaging algorithm. Much of the related work is carried out on the basis of backprojection imaging, and many imaging algorithms are modified on the basis of backprojection algorithms. Ref. [34] proposed a contour thinning imaging algorithm based on modulus stretch. This algorithm is an improvement on the backprojection algorithm, but can obtain a thinner contour than the traditional backprojection imaging. In recent years, research on CSAR imaging has been further developed. There have been many innovative research results [35–38].

In addition to imaging, target recognition is also an important aspect of CSAR research. In the early 1990s, researchers began to study automatic target recognition (ATR) on SAR [39–41]. At present, there is still a lot of research on SAR ATR. Due to the lack of experimental data, there are few studies on target recognition of CSAR and WSAR in the early stage. The Air Force Research Laboratory (AFRL) released a dataset in 2007. The dataset was obtained by airborne SAR during circular flight. This dataset is the first dataset about CSAR, also known as the Gotcha dataset. At the same time, AFRL also released challenging problems corresponding to the dataset [16]. In the second year, Dungan et al. proposed a target recognition algorithm based on point pattern matching. In the following years, Dungan et al. successively proposed several target recognition algorithms [42–44]. The algorithms proposed by Dungan et al. include a point pattern matching-based algorithm and a pyramid matching-based algorithm. In the case of using simple and easy data subsets, the algorithm proposed by Dungan et al. achieved good recognition results. In 2012, AFRL released the Target Discrimination Research Challenge and the corresponding dataset. This dataset is a subset of the Gotcha dataset, which was trimmed from a large scene, including 33 civilian vehicles and some auxiliary reflectors [19]. Since then, more researchers have begun to study target recognition with WSAR [45–54]. These target recognition algorithms, including feature set and template matching-based, manifold learning-based, and deep learning-based algorithms, have achieved good results.

Although there has been a great deal of research into SAR ATR, there is still little research on vehicle target recognition for wide-angle SAR. The existing recognition algorithms can be improved in terms of both efficiency and accuracy. Therefore, the study of wide-angle SAR target recognition is still meaningful. Combining imaging and target recognition is also a research direction in SAR and other radar detection fields. The combination target detection and imaging has also appeared in infrared target detection research [55–62]. In the previous work, the authors proposed a contour thinning imaging algorithm to improve target recognizability [34]. The algorithm combines imaging and target recognition. Based on contour thinning imaging, the authors also proposed a target recognition algorithm using feature set matching [53]. The contour thinning imaging algorithm significantly improved the target's recognizability, and achieved good results in vehicle recognition. This paper improves the contour thinning imaging algorithm. Although the contour thinning algorithm can obtain a clearer target contour, it still has disadvantages. After the contour is thinned, the target in the image loses some detailed information; in particular, block areas are obviously suppressed. This paper mainly is mainly aimed at improving the contour thinning imaging algorithm, so that it will lose less detailed information while maintaining contour thinning, and so that the target's recognizability will be increased. In addition to imaging, this paper uses convolutional neural network (CNN) to perform

target recognition on the improved images. The recognition results are used to verify whether the improved imaging algorithm is able to improve the accuracy of target recognition.

2. Imaging Algorithm

2.1. Analysis of Contour Thinning Imaging

The contour thinning algorithm was proposed in [34] and has been used in vehicle target recognition for CSAR [53]. This algorithm is based on the backprojection algorithm. The core idea is to stretch the modulus during the projection superposition process, highlight the areas with high modulus, and suppress the areas with low modulus, so as to obtain a contour thinning image. The main steps of the algorithm are given below [34].

The echo data received by the radar is a function of slow time τ_n and receiving frequency f_k, which is denoted by $S(f_k, \tau_n)$, where τ_n is the n-th sampling slow time, f_k is the k-th sampling frequency.

The IFFT transform is performed on $S(f_k, \tau_n)$ received at each τ_n to obtain an inverse transform sequence. The FFTshift(•) function is then used to shift the zero frequency point to the middle of the sequence.

$$s_0(m, \tau_n) = \text{FFTshift}\{\text{IFFT}[S(f_k, \tau_n)]\} \tag{1}$$

Let $\Delta R(\mathbf{r}, \tau)$ denote the difference between the distance from the origin to the radar and the distance from the target to the radar with the location $\mathbf{r}$ at time τ. Linear interpolation is performed on $s_0(m, \tau_n)$ to obtain the estimated values of the corresponding IFFT transformation at all $\Delta R(\mathbf{r}, \tau_n)$ points, and the sub-imaging data at each time τ_n is obtained by multiplying the data by the compensation term.

$$s_{int}(\mathbf{r}, \tau_n) = \text{Interp}[s_0(m, \tau_n)]\left(\frac{+j4\pi f_0 \Delta R(\mathbf{r}, \tau_n)}{c}\right), \tag{2}$$

$$S_{int}(\tau_n) = \left\{s_{int}(\mathbf{r}_{x,y}, \tau_n)\right\} \Big| x, y \in [1, L], \tag{3}$$

where L represents the side length of the imaging scene.

Let θ denote the size of the synthetic aperture of the SAR. All sub-images in the range of θ are superimposed. The function $\psi(\bullet)$ is then used to stretch the modulus for each sub-aperture image. The final image I can be obtained by superimposing all the sub-aperture images.

$$I = \sum_{\theta_i} \psi\left(\sum_{\tau_n \in \theta} S_{int}(\tau_n)\right) \tag{4}$$

$$\psi(x) = \begin{cases} k_1 x, & |x| \geq T \\ k_2 x, & |x| < T \end{cases}, \tag{5}$$

where k_1 and k_2 denote the enhancement coefficient and the inhibition coefficient, respectively. The T denotes the threshold value. Ref. [34] shows that the empirical values of k_1, k_2 and T are 1.2, 0.1 and 0.9, respectively.

Figure 1 shows an example of imaging results for three different vehicle models. Figure 1a–c shows the imaging results of using the traditional backprojection algorithm for three vehicle models, namely Chevrolet Impala LT, Mitsubishi Galant ES, and Toyota Highlander. Figure 1d–f corresponds to Figure 1a–c for the contour thinning imaging results. The value of θ during imaging is 10°. As can be seen from the figure, the results of contour thinning imaging are clearer than the results of traditional backprojection imaging, but the detailed information is also obviously lost, as shown by the red circle callout.

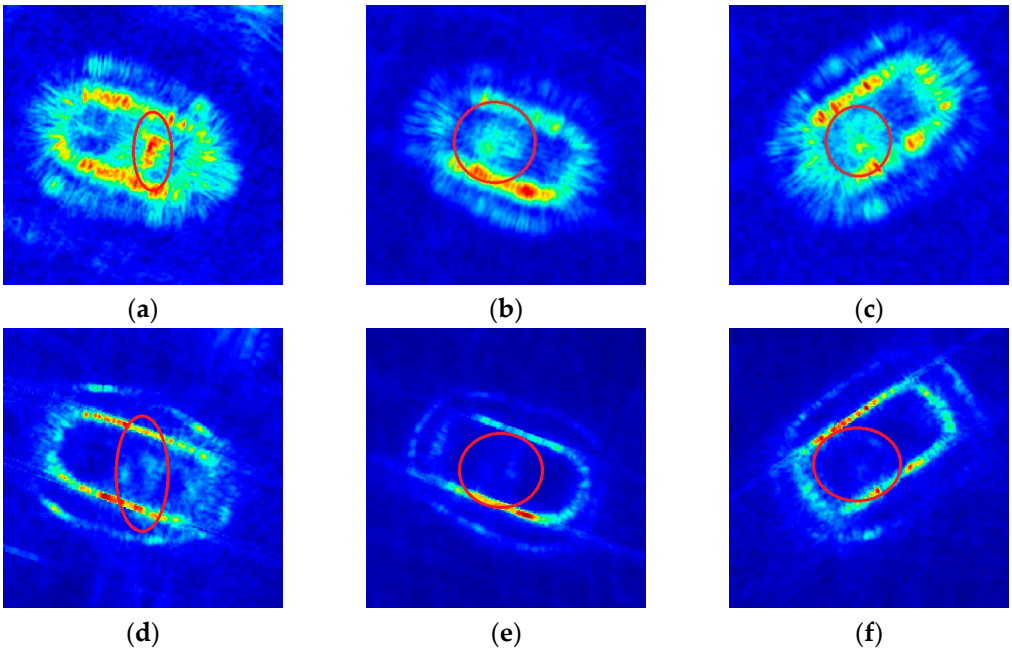


Figure 1. Example of imaging results of different models of vehicle targets in the Gotcha dataset by contour thinning imaging. (**a**–**c**) are images obtained by backprojection algorithm. (**d**–**f**) are images obtained by contour thinning algorithm. Three models of vehicle targets are used for imaging comparison: (**a**,**d**) Model Chevrolet Impala LT; (**b**,**e**) Model Mitsubishi Galant ES; (**c**,**f**) Model Toyota Highlander.

Figure 2 is a schematic of CSAR imaging. The missing details in the contour thinning image correspond to the high reflection parts of the front or rear of the vehicle, as shown in the left image in Figure 2. Obviously, not all vehicles have the same highly reflective contour in front or rear. Therefore, the loss of this part is likely to reduce the recognition of vehicle targets. The first task of this paper is to restore this missing part and compensate for it in the contour thinning image.

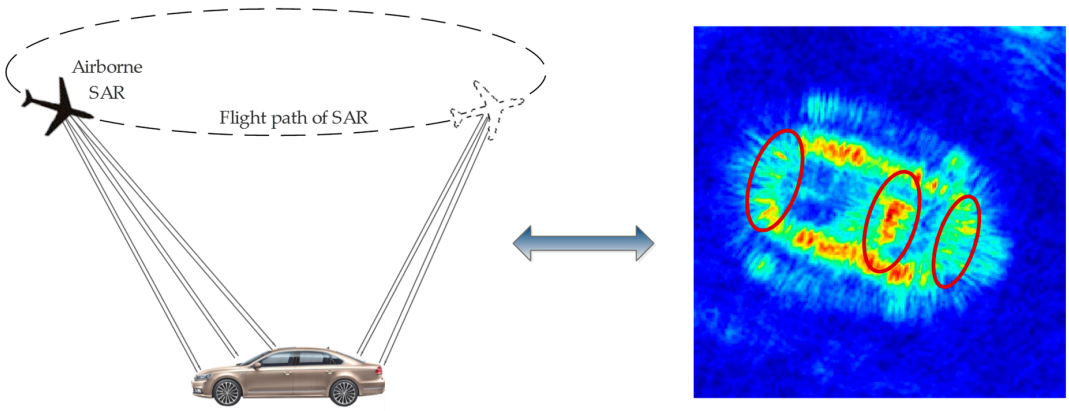


Figure 2. A diagram of circular SAR imaging. The picture on the left illustrates the process of airborne SAR flying around a ground target in a circle. The image on the right is the result of imaging the echo data using a backprojection algorithm. The part marked by the red circle in the right image corresponds to the high reflection part in the front or rear of the vehicle in the left image.

2.2. Residual Compensation

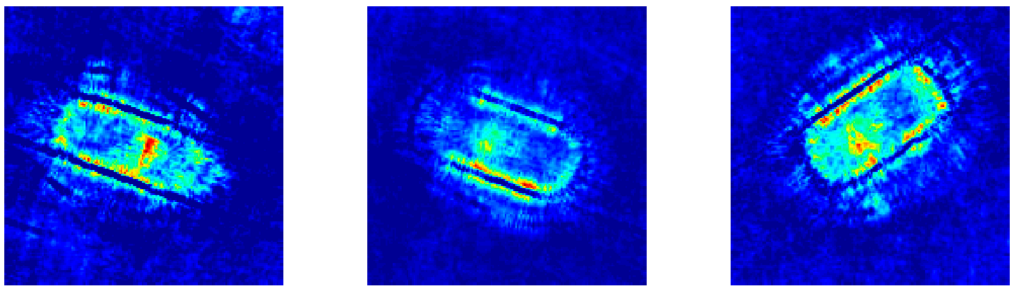
To retrieve the information lost during contour thinning imaging, compensation is considered. Because the image obtained by the backprojection algorithm can well restore the scattering characteristics of the target, in this paper we refer to the image obtained by the traditional backprojection algorithm

as the original image. The goal of compensation is to make the thinning contours correspond to all possible contours on the original image, and add the missing details to the thinning image. Let I_{org} denote the original image. Let I_{thin} denote the contour thinning image. The difference between I_{org} and I_{thin} is denoted by I_{res}, and is given by

$$\begin{aligned} I_{res} &= abs(I_{org} - I_{thin}) \\ &= \begin{bmatrix} \left|I_{org}(1,1) - I_{thin}(1,1)\right| & \left|I_{org}(1,2) - I_{thin}(1,2)\right| & \cdots & \left|I_{org}(1,L) - I_{thin}(1,L)\right| \\ \left|I_{org}(2,1) - I_{thin}(1,1)\right| & \left|I_{org}(2,2) - I_{thin}(2,2)\right| & \cdots & \left|I_{org}(2,L) - I_{thin}(1,L)\right| \\ \vdots & \vdots & \vdots & \vdots \\ \left|I_{org}(L,1) - I_{thin}(L,1)\right| & \left|I_{org}(L,2) - I_{thin}(L,2)\right| & \cdots & \left|I_{org}(L,L) - I_{thin}(L,L))\right| \end{bmatrix} \end{aligned} \tag{6}$$

where L denotes the pixel length of the image.

Figure 3 shows the example of residual image of different models of vehicles, corresponding to the difference between Figure 1a,d, Figure 1b,e, and Figure 1c,f, respectively.



(**a**) (**b**) (**c**)

Figure 3. Examples of residual image of different models of vehicles: (**a**) Model Chevrolet Impala LT, corresponding to the difference between Figure 1a,d; (**b**) Model Mitsubishi Galant ES, corresponding to the difference between Figure 1b,e; (**c**) Model Toyota Highlander, corresponding to the difference between Figure 1c,f.

Obviously, the missing details are contained in the residual image I_{res}. How to extract effective details from I_{res} and eliminate noise is a problem to be studied. Suppose the function that can achieve this requirement is represented by $\Phi(\bullet)$, the processed image can be expressed as

$$I_{cps} = \Phi(I_{res}) \tag{7}$$

When the image of compensation I_{cps} is obtained, it is superimposed with the thinning image I_{thin} to obtain the final compensated contour thinning image I_{fin}, which is given by

$$I_{fin} = I_{thin} + I_{cps} \tag{8}$$

In the process of compensation, the most important is the selection of $\Phi(\bullet)$. There are many ways to obtain the $\Phi(\bullet)$. For example, a method based on compressed sensing can be used to obtain the best signal under certain conditions. However, in the case of this paper, the main contour of the target has been successfully obtained, and the detailed information we want to extract is only the auxiliary information in the residual images. Therefore, after considering the computational complexity and cost performance, we prefer a simple image enhancement algorithm as the $\Phi(\bullet)$ function. Let's refocus on the goal of the function $\Phi(\bullet)$, which should be to preserve and enhance larger, brighter areas in the residual image while suppressing smaller, darker areas in the images. This is just a common speckle reduction problem in SAR image processing. There are several speckle reduction algorithms that can be used. In this paper, an algorithm with excellent performance in different scenarios is selected,

that is, the gravitation-based speckle reduction algorithm [53,63,64] is used as the $\Phi(\bullet)$ function. The gravitation-based speckle reduction algorithm is calculated as follows [53]:

$$\Phi(I(i,j)) = F(i,j) + G(i,j), F(i,j) = mI(i,j)^2, G(i,j) = \sum_{r \le R} m\frac{I(i,j)I(k,l)}{r^2}, \tag{9}$$

where $I(i, j)$ denotes the brightness of the point in the i-th row and the j-th column on image I. The $r = \sqrt{(i-k)^2 + (j-l)^2}$, representing the distance between (k, l) and (i, j). The radius of gravitational action is denoted by R. m is the coefficient of gravitation. $G(i, j)$ denotes the gravitational force of the surrounding point (i, j). $F(i, j)$ denotes the internal stress of point (i, j) itself. Ref. [53] shows that the empirical values of R and m are 10 and 1, respectively.

In practice, in order to get different degree of speckle reduction effect, $\Phi(\bullet)$ can be used several times iteratively, which is denoted by $\Phi^{(q)}(\bullet)$, where q is the number of iterations. For example:

$$\begin{aligned} \Phi^{(1)}(I(i,j)) &= \Phi(I(i,j)) \\ \Phi^{(2)}(I(i,j)) &= \Phi(\Phi(I(i,j))) \\ &\cdots\cdots \\ \Phi^{(n)}(I(i,j)) &= \underbrace{\Phi(\cdots\Phi(\Phi(I(i,j))))}_{\Phi(\bullet) \text{ iterates } n \text{ times}} \end{aligned} \tag{10}$$

In addition, the gravitation-based speckle reduction algorithm can also be used to denoise contour thinning image I_{thin}. However, this will increase the computation time, which can be optionally performed according to the actual situation. The processing procedure of the residual compensation imaging algorithm is shown in Algorithm 1.

Algorithm 1: Residual compensation imaging

Input:

Echo data $S(f_k, \tau_n)$, receiving frequency f_k, slow time τ_n.

FFT Points N_{fft}, slant range $\Delta R(\mathbf{r}, \tau)$, synthetic aperture θ, Image size L;

Output:

The compensated contour thinning image I_{fin}.

BEGIN
Initialize: $T = 0.9$, $k_1 = 1.2$, $k_2 = 0.1$, $R = 10$, $m = 1$, q.
Compute I_{org} and I_{thin} using Equations (1)–(5);
Denoiseing I_{thin} with Equation (9); (This step is optional)
$I_{res} = abs(I_{org} - I_{thin})$
while $q > 0$
  for $i = 1$ to L and $j = 1$ to L
    $I_{cps}(i,j) = m\sum_{r \le R} \frac{I_{res}(i,j)I_{res}(k,l)}{r^2} + mI_{res}(i,j)^2$;
  end for
  $I_{res} = I_{cps}$;
  $q = q - 1$;
end while
$I_{fin} = I_{thin} + I_{cps}$;
return I_{fin}.
END

3. Vehicle Target Recognition

The image after compensation contains more information than the image before compensation. However, it is not clear whether the added information is helpful to recognize the target. In this section, the convolutional neural networks (CNN) is used for vehicle target recognition. The detailed description of CNN is found in many papers and books [65,66], and will not be repeated here. This article briefly describes the steps of the algorithm used as follows:

(1) Linear coding and decoding are used for images in the library to obtain patch features through training. The image is cropped into patches of size 8×8, and then expanded into 64×1 vectors row by row. The vectors are input into a three-layer network, the input and output nodes of the network are 64, and the number of hidden layer nodes is variable. The function of this network is to make the output image as close to the input image as possible by training a large number of images. After the weight matrix converges, it can be used as the extracted features for subsequent convolution. When the number of hidden nodes is much less than the number of input nodes, it is also called sparse coding.

(2) Scale all images to standard size. All images are divided into training images and test images, and label data is generated at the same time. The training data set and the test data set are obtained respectively.

(3) The CNN is used to train the data in the training set. The network mainly includes two convolutions and pooling, and softmax regression at the output layer. In step (1), multiple 8×8 weight matrices obtained by linear coding are convolved with images of $L \times L$ size. The size after convolution is $(L - 7) \times (L - 7)$. The error is calculated for each training, and the corresponding network parameters are adjusted according to a certain criterion. Repeat the training until the error is small enough or the number of trainings exceeds the threshold.

(4) The network parameters obtained after the training is the optimal parameters. Use these parameters to recognize the images in the test set and calculate the accuracy.

The architecture of CNN used in this paper is shown in Figure 4.

The output layer of CNN uses softmax regression. The number of outputs is 6, which is the number of vehicle models. The loss function is shown as [66]:

$$J(y_i) = -\log \frac{e^{y_i}}{\sum_{k=1}^{6} e^{y_k}}, \tag{11}$$

where y_i denotes the output of the i-th neuron. There are many optimization algorithms for CNN. The optimization algorithm in this paper uses Limited-memory Broyden-Fletcher-Goldfarb-Shanno (L-BFGS) [67,68].

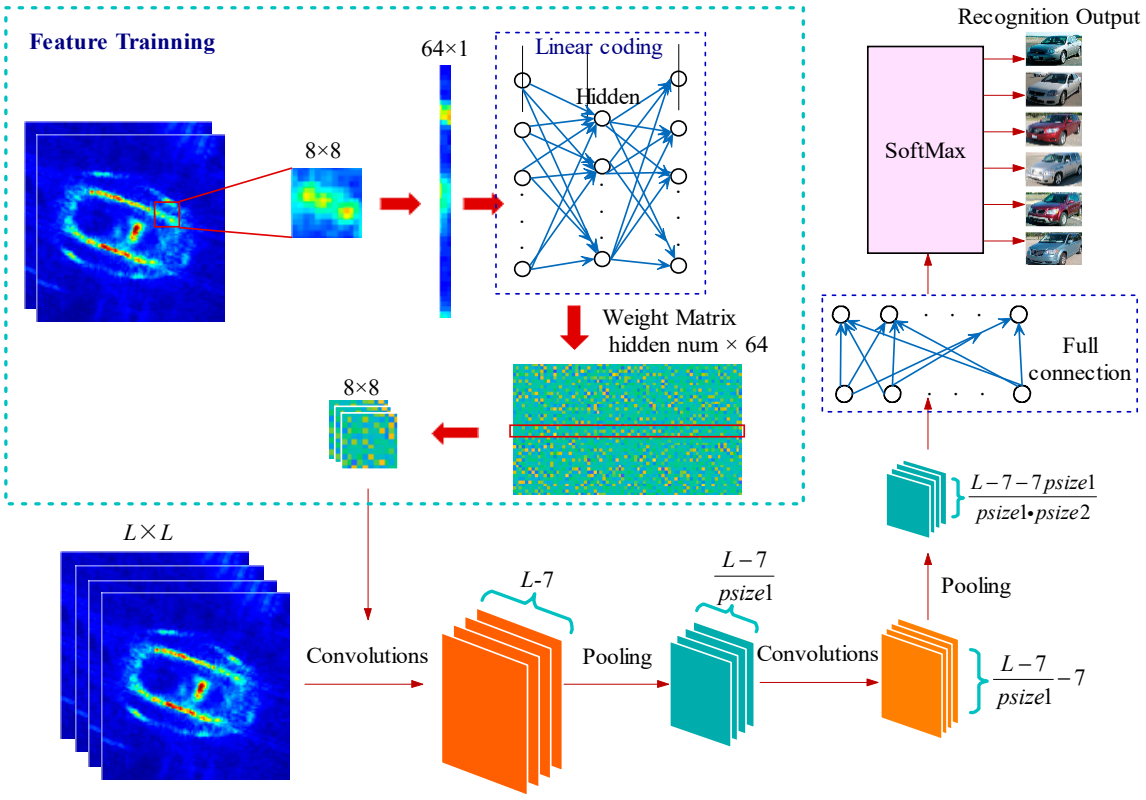


Figure 4. The architecture of convolutional neural networks (CNN) used in this paper. The input data is the residual compensation image of the vehicle target. The output of the network is the classification of vehicle targets. The network mainly includes feature training, convolution, pooling, and softmax regression.

In binary decision problems, the target is labeled as positive or negative. The decision made by the classifier can be represented as a confusion matrix. The confusion matrix has four categories: True positives (TP) are examples correctly labeled as positives. False positives (FP) refer to negative examples incorrectly labeled as positive. True negatives (TN) correspond to negatives correctly labeled as negative. False negatives (FN) refer to positive examples. There are usually 4 indicators used to evaluate the recognition results, namely *Accuracy*, *Precision*, *Sensitivity* (*Recall*) and *Specificity*, which are defined as follows [69]:

$$\begin{aligned} Accuracy &= \frac{TP+TN}{TP+TN+FP+FN}, \\ Precision &= \frac{TP}{TP+FP}, \\ Sensitivity = Recall &= \frac{TP}{TP+FN}, Specificity = \frac{TN}{TN+FP}. \end{aligned} \tag{12}$$

In multi-class decision problems, the above equations cannot be used directly. However, the accuracy can be intuitively obtained, that is, the sum of all the correct numbers that are identified is divided by the total number.

4. Experimental Results

The data used in the experiments in this paper comprise a subset of the Gotcha dataset released by AFRL, that is, the Target Discrimination Research subset [19]. Airborne SAR detects vehicle targets on the ground at 31 altitude orbits. The ground area is approximately 5 km in diameter. In each altitude

orbit, the airborne SAR makes circular flight around the ground area. Finally, 56 individual targets are extracted from the large dataset.

4.1. Residual Compensation Imaging

To get a better region of interest, the effect of speckle reduction under different iterations is compared, as shown in Figure 5. As can be seen from the figure, with the increase of iteration times, the bright areas become more concentrated and the noise is reduced. When the number of iterations is less than 2, the noise is relatively large, and the processed image is not suitable for direct compensation. When the iteration is more than three times, the noise is well suppressed. However, a large number of iterations will also erode the target, so it is appropriate to choose three or four iterations. In the following experiments, three iterations was selected, that is, $\Phi^{(3)}(\bullet)$ is selected as the extraction function.

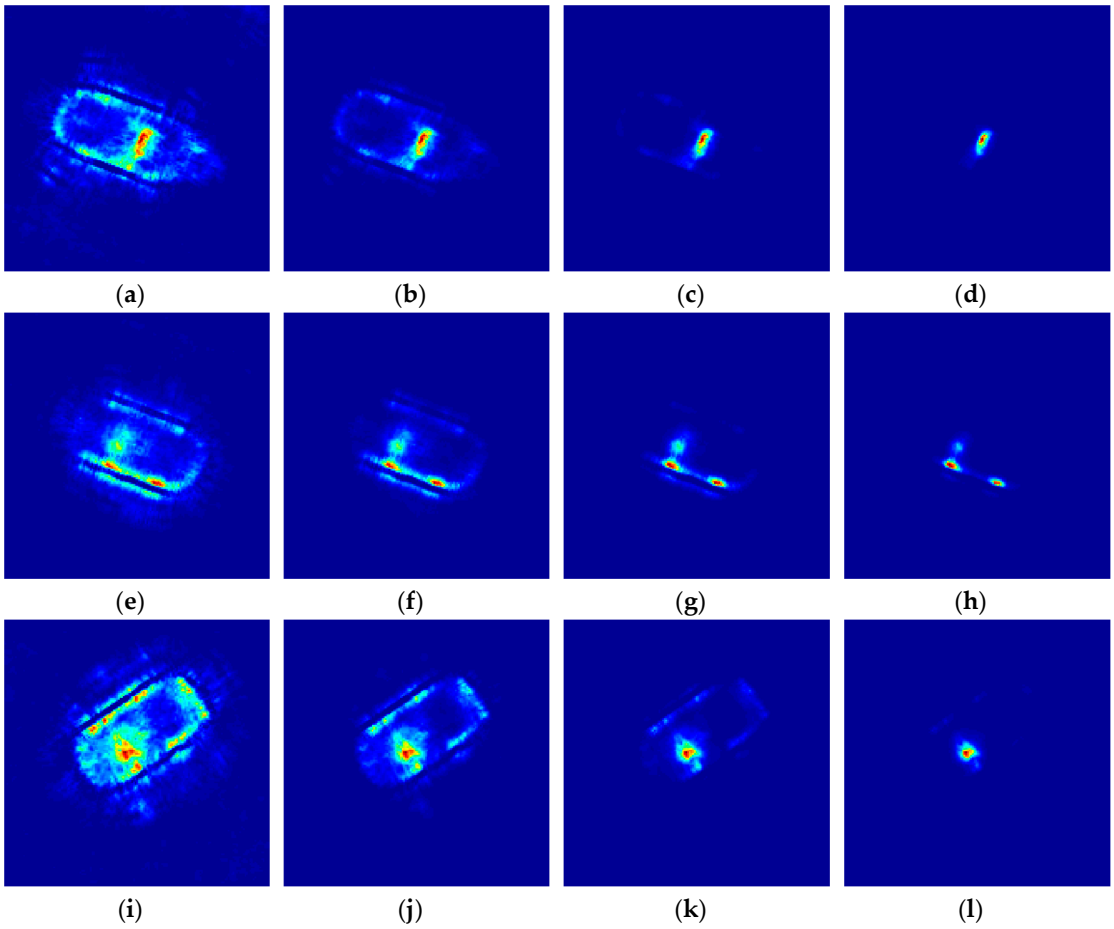


Figure 5. Examples of the speckle reduction effect of three vehicle models in different iteration times: (**a**–**d**) Model Chevrolet Impala LT, Corresponding to Figure 3a, iterated one to four times, respectively; (**e**–**h**) Model Mitsubishi Galant ES, Corresponding to Figure 3b, iterated one to four times, respectively; (**i**–**l**) Model Toyota Highlander, Corresponding to Figure 3c, iterated one to four times, respectively.

Figure 6 shows the comparison of I_{org}, I_{thin} and I_{fin} images of the three vehicle models in Figure 1a–c. Figure 6g–i are superimposed images of the contour thinning images and compensation images of the three vehicles. As can be seen from the figure, the compensated image adds detailed information and the contour is closer to the original image.

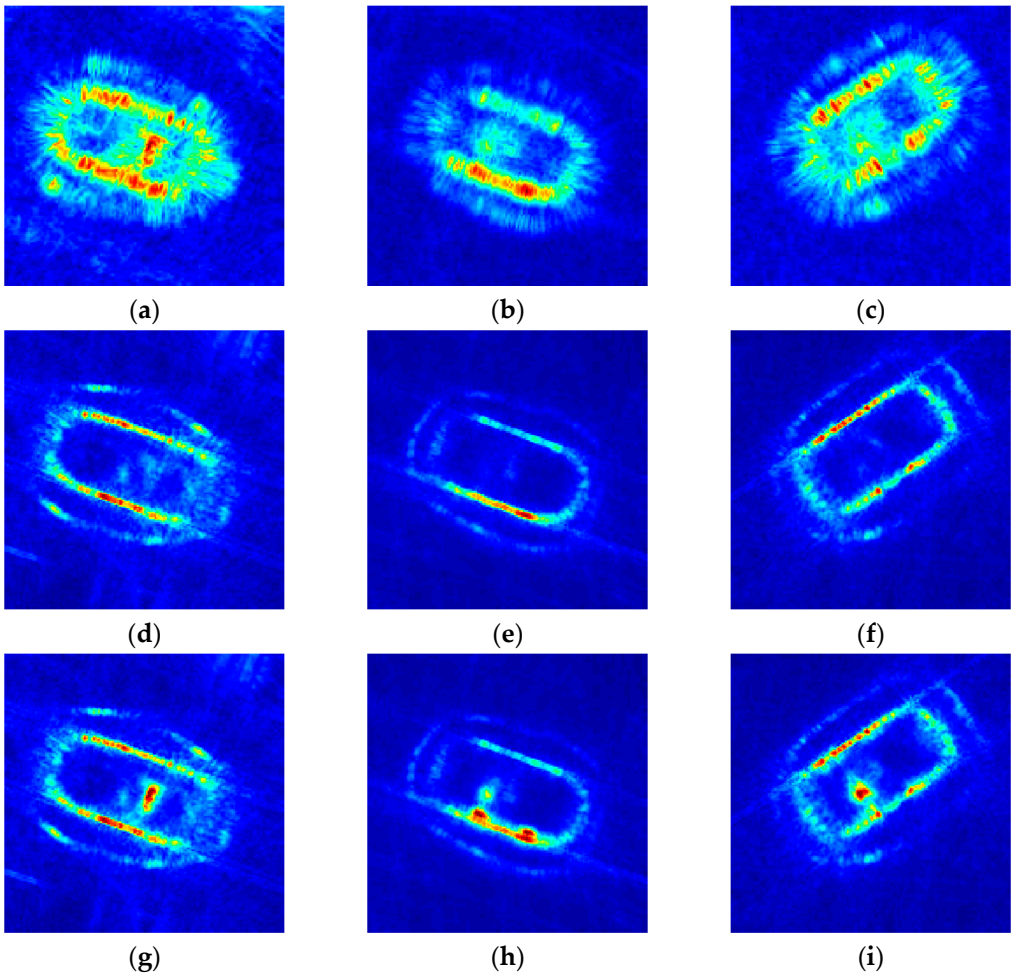


Figure 6. Comparison of I_{org}, I_{thin} and I_{fin} images of the three vehicle models of Chevrolet Impala LT, Mitsubishi Galant ES, and Toyota Highlander in Figure 1a–c: (**a**–**c**) I_{org} images of three vehicle models; (**d**–**f**) I_{thin} images of three vehicle models; (**g**–**i**) I_{fin} images of three vehicle models.

Ref. [34] gives an index of the contour thinning degree, which is denoted as $D(I)$. It is defined as the perimeter of the pixels of all the target areas in a binary image divided by the area of the pixels of all the target areas.

$$D(I) = \frac{\text{pixel perimeter of target}}{\text{pixel area of target}} \tag{13}$$

Similarly, the data of 150 vehicles randomly selected in the Gotcha dataset are imaged with synthetic apertures of 5°, 10°, and full aperture, respectively. Imaging methods include traditional backprojection, contour thinning, and residual compensation, which are denoted as I_{org}, I_{thin}, and I_{fin}. For each imaging method, the contour thinning degree $D(I)$ is calculated according to Equation (13), and the results are shown in Figure 7. As can be seen from the figure, the contour thinning degree after the residual compensation is basically the same as before compensation, and the area increased by compensation does not lower the contour thinning degree.

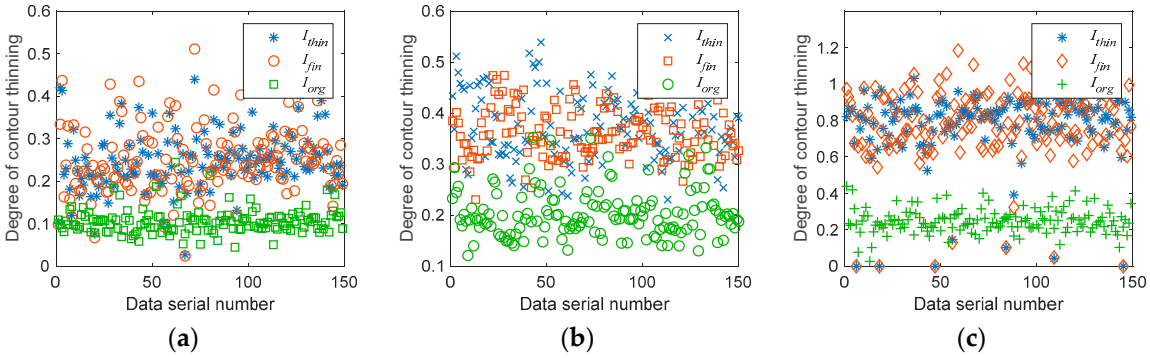


Figure 7. Comparison of contour thinning degree of backprojection imaging (I_{org}), contour thinning imaging (I_{thin}), and residual compensation imaging (I_{fin}): (**a**) 5° aperture imaging; (**b**) 10° aperture imaging; (**c**) Full aperture imaging.

4.2. Recognition Analysis

The dataset used for recognition is still the Target Discrimination Research subset of the Gotcha dataset [19]. In the process of radar detection, some vehicles have changed position, some doors or trunk opened. To reduce these interferences, only the data of the stationary vehicle is selected for the recognition experiment. Finally, 660 images from six models were used for recognition experiments. The names of the six models are Chevrolet Impala LT, Mitsubishi Galant ES, Toyota Highlander, Chevrolet HHR LT, Pontiac Torrent and Chrysler Town & Country respectively. The labels for these six models in the dataset are Fcara, Fcarb, Fsuv, Mcar, Msuv, and Van. The six vehicle models were represented in 80, 81, 143, 111, 103, and 142 images, respectively.

All images were randomly divided into training set and test set. Let β denote the ratio of the number of images in the training set to the total number of images. The training/testing ratio is $\beta/(1-\beta)$.

Tables 1–3 show the total confusion matrices of all models when β is 0.7 (corresponding training/testing ratio is 2.3) in an experiment. It can be clearly seen from the confusion matrix which vehicle model is more likely to be misidentified.

Table 1. The total confusion matrix for the recognition results of the test set in an experiment.

Input Model	Output Model					
	Fcara	**Fcarb**	**Fsuv**	**Mcar**	**Msuv**	**Van**
Fcara	20	0	2	0	2	0
Fcarb	1	21	2	0	0	0
Fsuv	0	1	34	2	1	5
Mcar	1	0	0	32	0	0
Msuv	0	0	0	1	30	0
Van	0	0	3	0	2	38

Table 2. The total confusion matrix for the recognition results of the trainning set in an experiment.

Input Model	Output Model					
	Fcara	**Fcarb**	**Fsuv**	**Mcar**	**Msuv**	**Van**
Fcara	56	0	0	0	0	0
Fcarb	0	57	0	0	0	0
Fsuv	0	0	99	1	0	0
Mcar	0	0	0	78	0	0
Msuv	0	1	0	0	71	0
Van	0	0	0	0	0	99

Table 3. The total confusion matrix for the recognition results of all images in an experiment.

Input Model	Output Model					
	Fcara	**Fcarb**	**Fsuv**	**Mcar**	**Msuv**	**Van**
Fcara	76	0	2	0	2	0
Fcarb	1	78	2	0	0	0
Fsuv	0	1	133	3	1	5
Mcar	1	0	0	110	0	0
Msuv	0	1	0	1	101	0
Van	0	0	3	0	2	137

Vehicle target recognition in this paper is a multi-class decision problem. For each model, it can be regarded as only a binary decision problem. That is, treat the model itself as positive, and treat others as negative. The total confusion matrix can be converted into six separate confusion matrices. The respective confusion matrices are shown in Tables 4–9 only for the test set.

Table 4. Confusion matrix for model Fcara in an experiment.

Predicted	Actual	
	Positive	**Negative**
Positive	20	2
Negative	4	172

Table 5. Confusion matrix for model Fcarb in an experiment.

Predicted	Actual	
	Positive	**Negative**
Positive	21	1
Negative	3	173

Table 6. Confusion matrix for model Fsuv in an experiment.

Predicted	Actual	
	Positive	**Negative**
Positive	34	7
Negative	9	148

Table 7. Confusion matrix for model Mcar in an experiment.

Predicted	Actual	
	Positive	**Negative**
Positive	32	1
Negative	3	162

Table 8. Confusion matrix for model Msuv in an experiment.

Predicted	Actual	
	Positive	**Negative**
Positive	30	5
Negative	1	162

Table 9. Confusion matrix for model Van in an experiment.

Predicted	Actual	
	Positive	**Negative**
Positive	38	5
Negative	5	150

According to Equation (12), the Accuracy, Precision, Sensitivity and Specificity of each model can also be calculated as shown in Table 10.

Table 10. The recognition indicators of each model were calculated based on the data in Tables 4–9.

Model	Accuracy (%)	Precision (%)	Sensitivity (%)	Specificity (%)
Fcara	97.0	90.9	83.3	98.9
Fcarb	98.0	95.5	87.5	99.4
Fsuv	91.9	82.9	79.1	95.5
Mcar	98.0	97.0	91.4	99.4
Msuv	97.0	85.7	96.8	97.0
Van	94.9	88.4	88.4	96.8

From the data in Table 10, the recognition accuracy looks pretty good. However, in fact, this is caused by simplifying the multi-class decision problem into a binary decision problem. In the binary decision process, many samples that are classified as negative and also identified as negative are actually identified incorrectly in multi-class decision. Therefore, the accuracy in Table 10 can be considered as artificially high. Let P denote the total accuracy of all models, defined as the ratio of the number of images recognized as the correct model in the dataset to the total number of images in the dataset. Let P_{all}, P_{test}, and P_{train} denote the accuracy of all images, the accuracy of the test set, and the accuracy of the training set, respectively. According to the data of the above experiment, P_{all}, P_{test} and P_{train} are 96.2%, 88.4% and 99.6%, respectively.

The data above is only the result of one experiment and is not representative. To analyze the recognition accuracy, subsequent experiments will be repeated multiple times to take the average. In the following experiments, each point in the figure is the average of the results of ten randomized trials.

Figure 8 shows the curve of accuracy changing with training set ratio β when CNN takes different number of hidden nodes. As can be seen from Figure 8a,c, the accuracy increases as β increases. However, when β is greater than 90%, the accuracy of the test set has a large deviation. When the number of hidden nodes is sufficient and the β is between 0.7 and 0.8, the accuracy of the test set is the highest, almost 90%. In Figure 8b, when the number of hidden nodes is large, the accuracy is almost 100%. However, when the number of hidden nodes is small, the accuracy of training set decreases with the increase of β. This is because fewer hidden nodes cannot extract accurate features. When the number of training samples increases, the extracted features will become worse, and the accuracy will decrease.

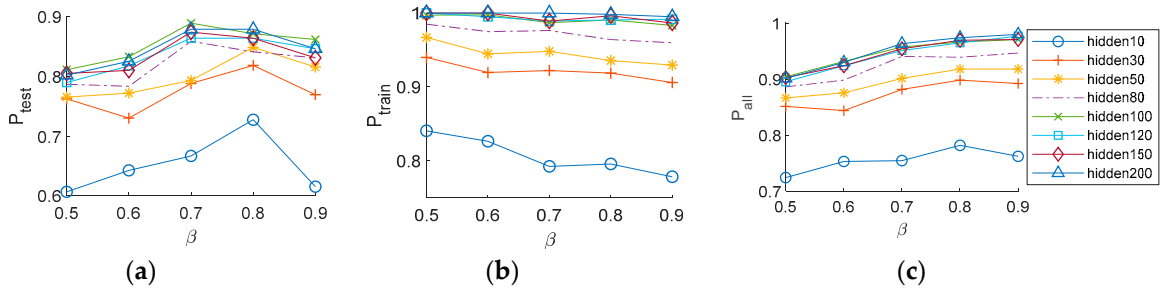


Figure 8. The curve of accuracy changing with training set ratio β when CNN takes different number of hidden nodes. The horizontal axis in the figure represents the proportion of the number of training images to the total number of images. The vertical axis represents the recognition accuracy: (**a**) The accuracy of the test set; (**b**) The accuracy of the training set; (**c**) The accuracy of all images.

Figure 9 shows the curve of accuracy changing with the number of hidden nodes in CNN at different β. As can be seen from the figure, when the number of hidden nodes exceeds 100, the accuracy is generally stable, and does not increase significantly as the number of nodes increases. When the number of hidden nodes is greater than 100, the test accuracy P_{test} is almost greater than 80%, the training accuracy P_{train} is close to 100%, and the total accuracy P_{all} is greater than 90%. When the number of hidden nodes is 100 and β is 0.7, the test accuracy P_{test} has the highest value of 89%.

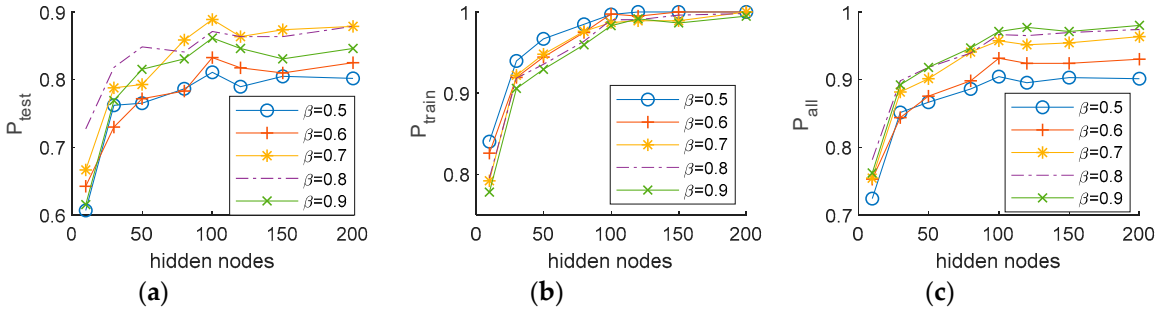


Figure 9. The curve of accuracy changing with the number of hidden nodes in CNN at different β. The horizontal axis in the figure represents the hidden nodes in CNN. The vertical axis represents the recognition accuracy: (**a**) The accuracy of the test set; (**b**) The accuracy of the training set; (**c**) The accuracy of all images.

Figures 10 and 11 show the recognition accuracy curves of each model of vehicle. Figure 10 shows the accuracy of each model changing with training set ratio β. Figure 11 shows the accuracy of each model changing with the number of hidden nodes in CNN. It can be seen from the figure that which model of vehicle is more easily recognized and which model of vehicle is more easily confused. That is, model Mcar has higher recognition accuracy, while model Fcarb has lower recognition accuracy.

Figure 12 show the examples of residual compensation imaging for six models of vehicles. As can be intuitively seen from the figure, some of the differences between different models of vehicles are small, while others are obvious.

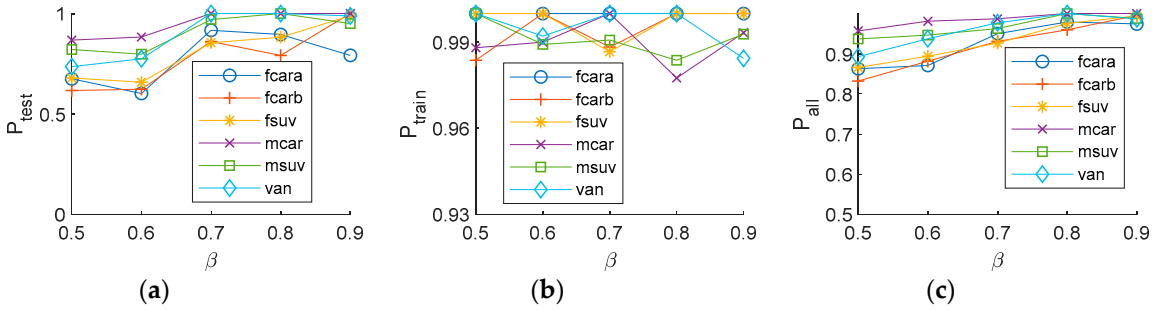


Figure 10. The accuracy of each model changing with training set ratio β. The horizontal axis in the figure represents the proportion of the number of training images to the total number of images. The vertical axis represents the recognition accuracy: (**a**) The accuracy of the test set; (**b**) The accuracy of the training set; (**c**) The accuracy of all images.

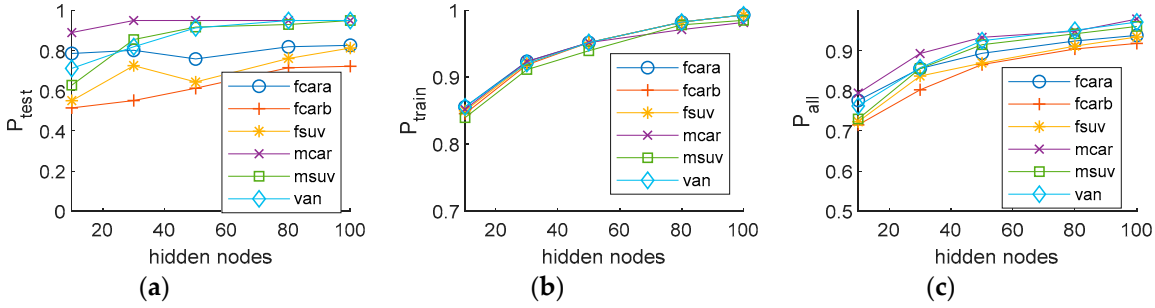


Figure 11. The accuracy of each model changing with the number of hidden nodes in CNN. The horizontal axis in the figure represents the hidden nodes in CNN. The vertical axis represents the recognition accuracy: (**a**) The accuracy of the test set; (**b**) The accuracy of the training set; (**c**) The accuracy of all images.

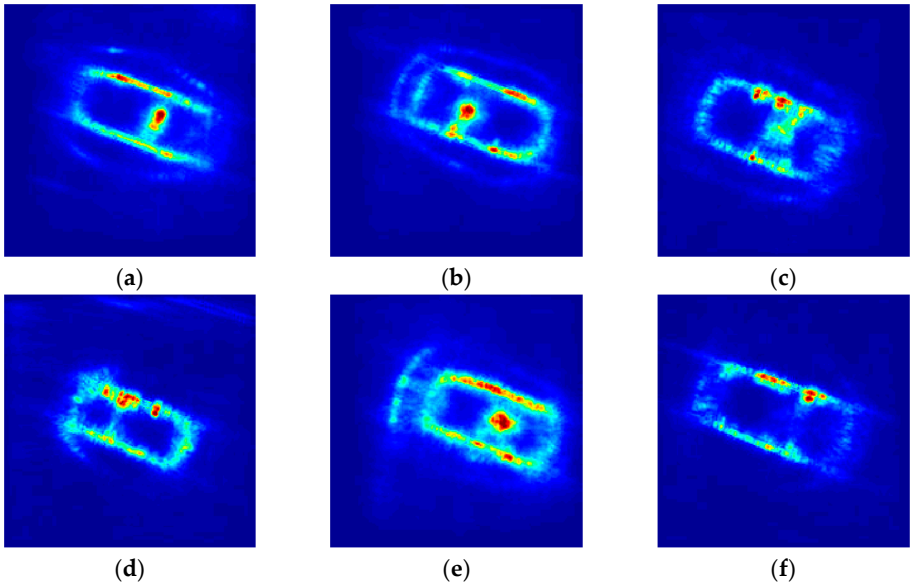


Figure 12. Examples of residual compensation imaging for six models of vehicles: (**a**) Model Chevrolet Impala LT, the label in the dataset is Fcara; (**b**) Model Mitsubishi Galant ES, the label in the dataset is Fcarb; (**c**) Model Toyota Highlander, the label in the dataset is Fsuv; (**d**) Model Chevrolet HHR LT, the label in the dataset is Mcar; (**e**) Model Pontiac Torrent, the label in the dataset is Msuv; (**f**) Model Chrysler Town & Country, the label in the dataset is Van.

In the above experiment, the size of the images was 100 × 100. Figure 13 shows the comparison of the test accuracy of the compensated image I_{fin} and the contour thinning image I_{thin} changing with the image size L.

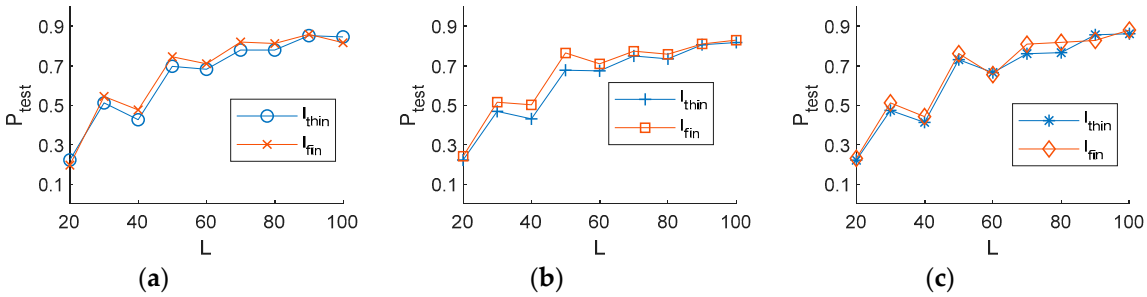


Figure 13. The comparison of the test accuracy of the original image and the contour thinning image changing with the image size. The horizontal axis in the figure represents the image size. The unit of the abscissa is pixel. The vertical axis represents the recognition accuracy: (**a**) The training images ratio β is 0.5; (**b**) The training images ratio β is 0.6; (**c**) The training images ratio β is 0.7.

As can be seen from Figure 13, the accuracy increases as the image size increases. When the image size is less than 40 × 40, the accuracy is very low, just like random guess. When the image size is larger than 70 × 70, the accuracy tends to be stable, and increasing the image size has a limited improvement in accuracy. In almost all cases, the image recognition accuracy of I_{fin} is higher than that of I_{thin}. Experiment results show that the compensated image improves the recognition accuracy by about 3% on average.

5. Discussion

There have been many studies on CSAR imaging algorithms. Most of these studies have focused on accurately reducing the scattering characteristics of targets. The contour thinning imaging algorithm in this paper is not for the purpose of accurately reducing the scattering characteristics of the target, but for the purpose of enhancing the recognizability of the target. Residual compensation imaging algorithm proposed in this paper is to further improve and highlight the contour characteristics of the target on the basis of contour thinning. Therefore, this paper does not use other papers' commonly used signal-to-noise ratio, peak side lobe ratio and other indicators to evaluate the image results. To compare with the previous work, the contour thinning degree is used to quantify the contour characteristics of the imaging results. However, the contour thinning degree is only a secondary indicator; more important is the impact of imaging results on target recognition. Therefore, CNN was used to test different imaging results, and the experimental results showed that the residual compensation imaging algorithm could indeed improve the accuracy of target recognition.

At present, little research has been done on vehicle model recognition using the Gotcha dataset. There are only a few papers on vehicle target recognition with WSAR. The earlier study of vehicle target recognition of CSAR on the Gotcha dataset was conducted by Dungan et al. They used a point set to represent the vehicle image, used the Mahalanobis distance as a measure between the point sets, and applied algorithms such as point pattern matching and pyramid hash matching to recognize the vehicle model, and achieved a recognition accuracy of more than 95% [42,44]. However, the data used by Dungan et al. and the data in this paper are two different subsets of Gotcha dataset. The data used by Dungan et al. are eight groups of altitude orbit data of the same vehicle at the same location. The data used in this paper includes data for different vehicles, different locations and 31 altitude orbits. Gianelli et al. used the same subset of the Gotcha dataset for vehicle target recognition research, and their proposed recognition algorithm achieved a recognition accuracy of 90% [45]. However, in their experiment, they removed many of the flawed images and kept only 540 images of vehicles for recognition. In this paper, only the moving and changing image data of the vehicle is excluded.

The number of images actually used for recognition experiments is 660. Based on the above situation, this paper mainly analyzes the impact of imaging results on the recognition accuracy, and does not compare with the recognition accuracy of other recognition algorithms.

6. Conclusions

This paper presents an improved contour thinning imaging algorithm based on residual compensation for CSAR. The algorithm adds a compensation module to the contour thinning imaging algorithm, which better restores the original scattering characteristics of the target. The imaging results show that the image after compensation does not reduce the contour thinning degree, and contains more information than the image before compensation. To verify the influence of the residual compensation imaging algorithm on target recognition, the convolutional neural network is used to recognize vehicle targets. Experiment results show that the image after compensation has a higher target recognition accuracy than the image before compensation. The improved accuracy is about 3% on average. The proposed algorithm is demonstrated on the Gotcha dataset. The residual compensation imaging algorithm proposed in this paper is simple and easy to understand. This algorithm can effectively obtain a clear and complete vehicle contour image, and improve the recognizability of the target. Although the algorithm proposed in this paper is obtained from CSAR data, it can be extended to common WSAR data with detection angles of less than 360°. In our future work, we will focus on the integration of imaging, focusing and target recognition to further improve the accuracy of target recognition.

Author Contributions: Conceptualization, R.H.; Formal analysis, R.H. and J.M.; Funding acquisition, Z.P.; Investigation, R.H., J.M. and W.L.; Methodology, R.H.; Project administration, Z.P.; Software, R.H.; Supervision, Z.P.; Visualization, R.H.; Writing—original draft, R.H.; Writing—review and editing, Z.P. All authors have read and agreed to the published version of the manuscript.

Funding: This work is supported by National Natural Science Foundation of China (61775030, 61571096), Sichuan Science and Technology Program (2019YJ0167) and Open Research Fund of Key Laboratory of Optical Engineering, Chinese Academy of Sciences (2017LBC003).

Acknowledgments: The authors thank the Air Force Research Laboratory (AFRL) for the experimental dataset. The authors would like to thank the Laboratory of Imaging Detection and Intelligent Perception, School of Information and Communication Engineering, University of Electronic Science and Technology of China for providing the experiment condition. The authors thank Xingguo Liu (University of Electronic Science and Technology of China) and Kelong Zheng (Southwest University of Science and Technology) for their useful advice during this work. The authors thank reviewers for the valuable comments.

Conflicts of Interest: The authors declare no conflict of interest.

References

1. Peng, Z.; Zhang, J.; Meng, F.; Dai, J. Time-frequency analysis of SAR image based on generalized S-Transform. In Proceedings of the 2009 International Conference on Measuring Technology and Mechatronics Automation (ICMTMA2009), Zhangjiajie, China, 11–12 April 2009; Volume 1, pp. 556–559.
2. Peng, Z.; Wang, H.; Zhang, G.; Yang, S. Spotlight SAR images restoration based on tomography model. In Proceedings of the 2009 Asia-Pacific Conference on Synthetic Aperture Radar, APSAR 2009, Xian, China, 26–30 October 2009; pp. 1060–1063.
3. Peng, Z.; Liu, S.; Tian, G.; Chen, Z.; Tao, T. Bridge detection and recognition in remote sensing SAR images using pulse coupled neural networks. In Proceedings of the 7th International Symposium on Neural Networks, ISNN 2010, Shanghai, China, 6–9 June 2010; Volume 67, pp. 311–320.
4. Tao, T.; Peng, Z.; Yang, C.; Wei, F.; Liu, L. Targets detection in SAR image used coherence analysis based on S-transform. In *Electrical Engineering and Control*; Springer: Berlin/Heidelberg, Germany, 2011; Volume 98, pp. 1–9.
5. Yang, J.; Peng, Z. SAR target recognition based on spectrum feature of optimal gabor transform. In Proceedings of the International Conference on Communications, Circuits and Systems (ICCCAS2013), Chengdu, China, 15–17 November 2013; Volume 2, pp. 230–234.

6. Liu, Y.; Peng, L.; Huang, S.; Wang, X.; Wang, Y.; Peng, Z. River detection in high-resolution SAR data using the Frangi filter and Shearlet feature. *Remote Sens. Lett.* **2019**, *10*, 949–958. [CrossRef]
7. Huang, P.; Li, K.; Xu, W.; Tan, W.; Gao, Z.; Li, Y. Focusing arc-array bistatic synthetic aperture radar data based on keystone transform. *Electronics* **2019**, *8*, 1389. [CrossRef]
8. Li, G.; Lu, Q.; Lao, G.; Ye, W. Wideband noise interference suppression for sparsity-based SAR imaging based on dechirping and double subspace extraction. *Electronics* **2019**, *8*, 1019. [CrossRef]
9. Wang, Z.; Liu, M.; Lv, K. Retrieval of three-dimensional surface deformation using an improved differential SAR tomography system. *Electronics* **2019**, *8*, 174. [CrossRef]
10. Gao, B.; Li, X.; Sun, J.; Wu, J. Modeling of high-resolution data converter: Two-step pipelined-SAR ADC based on ISDM. *Electronics* **2020**, *9*, 137. [CrossRef]
11. Liu, Y.; Zhang, P.; He, Y.; Peng, Z. River detection based on feature fusion for synthetic aperture radar images. *J. Appl. Remote Sens.* **2020**, *14*, 016505. [CrossRef]
12. Jin, M.; Chen, M. Analysis and simulation for a spotlight-mode aircraft SAR in circular flight path. In Proceedings of the 13th Annual International Geoscience and Remote Sensing Symposium, Tokyo, Japan, 18–21 August 1993; Volume 4, pp. 1777–1780.
13. Wang, Z.; Wang, Z.; Xu, J. The effect of the attitude of the circular orbiting SAR on doppler properties. *Int. J. Remote Sens.* **1994**, *15*, 2313–2322. [CrossRef]
14. Broquetas, A.; Deporrata, R.; Sagues, L.; Fabregas, X.; Jofre, L. Circular Synthetic Aperture Radar (C-SAR) system for ground-based applications. *Electron. Lett.* **1997**, *33*, 988–989. [CrossRef]
15. Soumekh, M. Reconnaissance with slant plane circular SAR imaging. *IEEE Trans. Image Process.* **1996**, *5*, 1252–1265. [CrossRef]
16. Casteel, J.C.H.; Gorham, L.A.; Minardi, M.J.; Scarborough, S.M.; Naidu, K.D.; Majumder, U.K. A challenge problem for 2D/3D imaging of targets from a volumetric data set in an urban environment. In Proceedings of the Algorithms for Synthetic Aperture Radar Imagery XIV; International Society for Optics and Photonics, Orlando, FL, USA, 10–11 April 2007; Volume 6568.
17. Ertin, E.; Austin, C.D.; Sharma, S.; Moses, R.L.; Potter, L.C. GOTCHA experience report: Three-dimensional SAR imaging with complete circular apertures. In Proceedings of the Algorithms for Synthetic Aperture Radar Imagery XIV, Orlando, FL, USA, 10–11 April 2007; Volume 6568.
18. Gorham, L.A.; Moore, L.J. SAR image formation toolbox for MATLAB. In Proceedings of the Algorithms for Synthetic Aperture Radar Imagery XVII, Orlando, FL, USA, 8–9 April 2010; Volume 7699.
19. Dungan, K.E.; Ash, J.N.; Nehrbass, J.W.; Parker, J.T.; Gorham, L.A.; Scarborough, S.M. Wide angle SAR data for target discrimination research. In Proceedings of the Algorithms for Synthetic Aperture Radar Imagery XIX, Baltimore, MD, USA, 25–26 April 2012; Volume 8394.
20. Cantalloube, H.M.J.; Colin-Koeniguer, E.; Oriot, H. High resolution SAR imaging along circular trajectories. *Int. Geosci. Remote Sens. Symp.* **2007**, 850–853. [CrossRef]
21. Tan, W.X.; Wang, Y.P.; Wen, H.; Wu, Y.R.; Li, N.J.; Hu, C.F.; Zhang, L.X. Circular SAR experiment for human body imaging. In Proceedings of the 1st Asian And Pacific Conference on Synthetic Aperture Radar, Huangshan, China, 5–9 November 2007; pp. 90–93.
22. Lin, Y.; Hong, W.; Tan, W.X.; Wang, Y.P.; Wu, Y.R. Interferometric circular SAR method for three-dimensional imaging. *IEEE Geosci. Remote Sens. Lett.* **2011**, *8*, 1026–1030. [CrossRef]
23. Lin, Y.; Hong, W.; Tan, W.X.; Wu, Y.R. Extension of range migration algorithm to squint circular SAR imaging. *IEEE Geosci. Remote Sens. Lett.* **2011**, *8*, 651–655. [CrossRef]
24. Lin, Y.; Hong, W.; Tan, W.X.; Wang, Y.P.; Xiang, M.S. Airborne Circular Sar Imaging: Results at P-Band. In Proceedings of the International Geoscience and Remote Sensing Symposium, Munich, Germany, 22–27 July 2012; pp. 5594–5597.
25. Zhao, Y.; Lin, Y.; Hong, W.; Yu, L.J. Adaptive imaging of anisotropic target based on circular-SAR. *Electron. Lett.* **2016**, *52*, 1406–1407. [CrossRef]
26. Xue, F.; Lin, Y.; Hong, W.; Yin, Q.; Zhang, B.; Shen, W.; Zhao, Y. Analysis of azimuthal variations using multi-aperture polarimetric entropy with circular SAR images. *Remote Sens.* **2018**, *10*, 123. [CrossRef]
27. Shen, W.; Lin, Y.; Yu, L.; Xue, F.; Hong, W. Single channel circular SAR moving target detection based on logarithm background subtraction algorithm. *Remote Sens.* **2018**, *10*, 742. [CrossRef]
28. Teng, F.; Hong, W.; Lin, Y. Aspect entropy extraction using circular SAR data and scattering anisotropy analysis. *Sensors* **2019**, *19*, 346. [CrossRef] [PubMed]

29. Kou, L.; Wang, X.; Xiang, M.; Zhu, M. High sidelobe effects on interferometric coherence for circular SAR imaging geometry. *J. Syst. Eng. Electron.* **2013**, *24*, 76–83. [CrossRef]
30. Kou, L.; Xiang, M.; Wang, X.; Zhu, M. Tropospheric effects on L-band geosynchronous circular SAR imaging. *IET Radar Sonar Navig.* **2013**, *7*, 693–701. [CrossRef]
31. Kou, L.; Wang, X.; Xiang, M. Effects on three-dimensional geosynchronous circular SAR imaging by orbit errors. *J. Indian Soc. Remote Sens.* **2014**, *42*, 1–12. [CrossRef]
32. Yuan, X.; Ternovskiy, I. Improved image reconstruction from sub-apertures of circular spotlight SAR. In *Cyber Sensing 2015*; International Society for Optics and Photonics: Santa Clara, CA, USA, 2015; Volume 9458, p. 945802.
33. Chen, L.; An, D.; Huang, X.; Zhou, Z. A 3D reconstruction strategy of vehicle outline based on single-pass single-polarization CSAR data. *IEEE Trans. Image Process.* **2017**, *26*, 5545–5554. [CrossRef]
34. Hu, R.; Peng, Z.; Zheng, K. Modulus stretch-based circular SAR imaging with contour thinning. *Appl. Sci.* **2019**, *9*, 2728. [CrossRef]
35. Xie, H.; Shi, S.; An, D.; Wang, G.; Wang, G.; Xiao, H.; Huang, X.; Zhou, Z.; Xie, C.; Wang, F.; et al. Fast factorized backprojection algorithm for one-stationary bistatic spotlight circular SAR image formation. *IEEE J. Sel. Top. Appl. Earth Obs. Remote Sens.* **2017**, *10*, 1494–1510. [CrossRef]
36. Liu, T.; Pi, Y.; Yang, X. Wide-angle CSAR imaging based on the adaptive subaperture partition method in the terahertz band. *IEEE Trans. Terahertz Sci. Technol.* **2018**, *8*, 165–173. [CrossRef]
37. Wu, B.; Gao, Y.; Ghasr, M.T.; Zoughi, R. Resolution-based analysis for optimizing subaperture measurements in circular SAR imaging. *IEEE Trans. Instrum. Meas.* **2018**, *67*, 2804–2811. [CrossRef]
38. Du, B.; Qiu, X.; Huang, L.; Lei, S.; Lei, B.; Ding, C. Analysis of the azimuth ambiguity and imaging area restriction for circular SAR based on the back-projection algorithm. *Sensors* **2019**, *19*, 4920. [CrossRef] [PubMed]
39. Burl, M.C.; Owirka, G.J.; Novak, L.M. Texture discrimination in synthetic aperture radar imagery. In Proceedings of the Asilomar Conference on Circuits, Systems & Computers, Pacific Grove, CA, USA, 30 October–1 November 1989; Volume 1, pp. 399–404.
40. Mahalanobis, A.; Forman, A.V.; Bower, M.R.; Day, N.; Cherry, R.F. Quadratic distance classifier for multiclass SAR ATR using correlation filters. *Ultrah. Resolut. Radar* **1993**, *1875*, 84–95.
41. Novak, L.M.; Owirka, G.J.; Netishen, C.M. Performance of a high-resolution polarimetric SAR automatic target recognition system. *Linc. Labor. J.* **1993**, *6*, 11–24.
42. Dungan, K.E.; Potter, L.C.; Blackaby, J.; Nehrbass, J. Discrimination of civilian vehicles using wide-angle SAR. In Proceedings of the SPIE Defense and Security Symposium, Orlando, FL, USA, 17–18 March 2008; Volume 6970.
43. Dungan, K.E.; Potter, L.C. Effects of polarization on wide-angle SAR classification performance. In Proceedings of the 2010 IEEE National Aerospace Electronics Conference, Fairborn, OH, USA, 14–16 July 2010; pp. 50–53.
44. Dungan, K.E.; Potter, L.C. Classifying vehicles in wide-angle radar using pyramid match hashing. *IEEE J. Sel. Top. Signal Process.* **2011**, *5*, 577–591. [CrossRef]
45. Gianelli, C.D.; Xu, L. Focusing, imaging, and atr for the gotcha 2008 wide angle sar collection. In Proceedings of the Algorithms for Synthetic Aperture Radar Imagery XX, Baltimore, MD, USA, 1–2 May 2013; Volume 8746.
46. Ertin, E. Manifold learning methods for wide-angle SAR ATR. In Proceedings of the 2013 International Conference on Radar—Beyond Orthodoxy: New Paradigms in Radar, Adelaide, Australia, 9–12 September 2013; pp. 500–504.
47. Saville, M.A.; Jackson, J.A.; Fuller, D.F. Rethinking vehicle classification with wide-angle polarimetric SAR. *Aerosp. Electron. Syst. Mag.* **2014**, *29*, 41–49. [CrossRef]
48. Wagner, S.A. SAR ATR by a combination of convolutional neural network and support vector machines. *IEEE Trans. Aerosp. Electron. Syst.* **2016**, *52*, 2861–2872. [CrossRef]
49. Chen, S.; Wang, H.; Xu, F.; Jin, Y. Target classification using the deep convolutional networks for SAR images. *IEEE Trans. Geosci. Remote Sens.* **2016**, *54*, 4806–4817. [CrossRef]
50. Kechagias-Stamatis, O.; Aouf, N. Fusing deep learning and sparse coding for SAR ATR. *IEEE Trans. Aerosp. Electron. Syst.* **2018**, *55*, 785–797. [CrossRef]
51. Kechagias-Stamatis, O. Target recognition for synthetic aperture radar imagery based on convolutional neural network feature fusion. *J. Appl. Remote Sens.* **2018**, *12*, 046025. [CrossRef]

52. Li, Y.; Jin, Y. Target decomposition and recognition from wide-angle SAR imaging based on a Gaussian amplitude-phase model. *Sci. China Inf. Sci.* **2017**, *60*, 062305. [CrossRef]
53. Hu, R.; Peng, Z.; Ma, J. A vehicle target recognition algorithm for wide-angle SAR based on joint feature set matching. *Electronics* **2019**, *8*, 1252. [CrossRef]
54. Hu, R.; Peng, Z.; Ma, J. Vehicle target discrimination algorithm for wide-angle SAR based on loose iterative MDS. In Proceedings of the 8th Applied Optics and Photonics China (AOPC 2019), Beijing, China, 7–9 July 2019; Volume 11338.
55. Liu, X.; Chen, Y.; Peng, Z.; Wu, J. Infrared image super-resolution reconstruction based on quaternion and high-order overlapping group sparse total variation. *Sensors* **2019**, *19*, 5139. [CrossRef]
56. Zhang, L.; Peng, Z. Infrared small target detection based on partial sum of tensor nuclear norm. *Remote Sens.* **2019**, *11*, 382. [CrossRef]
57. Zhang, T.; Wu, H.; Liu, Y.; Peng, L.; Yang, C.; Peng, Z. Infrared small target detection based on non-convex optimization with L_p-norm constraint. *Remote Sens.* **2019**, *11*, 559. [CrossRef]
58. Peng, L.; Zhang, T.; Liu, Y.; Li, M.; Peng, Z. Infrared dim target detection using shearlet's kurtosis maximization under non-uniform background. *Symmetry* **2019**, *11*, 723. [CrossRef]
59. Peng, L.; Zhang, T.; Huang, S.; Pu, T.; Liu, Y.; Lyv, Y.; Zheng, Y.; Peng, Z. Infrared small target detection based on multi-directional multi-scale high boost response. *Opt. Rev.* **2019**, *26*, 568–582. [CrossRef]
60. Huang, S.; Liu, Y.; He, Y.; Zhang, T.; Peng, Z. Structure adaptive clutter suppression for infrared small target detection: Chain-growth filtering. *Remote Sens.* **2020**, *12*, 47. [CrossRef]
61. Lyv, Y.; Peng, L.; Pu, T.; Yang, C.; Peng, Z. Cirrus detection based on RPCA and fractal dictionary learning in infrared imagery. *Remote Sens.* **2020**, *12*, 142.
62. Guan, X.; Peng, Z.; Huang, S.; Chen, Y. Gaussian scale-space enhanced local contrast meansure for small infrared target detection. *IEEE Geosci. Remote Sens. Lett.* **2020**, *17*, 327–331. [CrossRef]
63. Tian, S.; Sun, G.; Wang, C.; Zhang, H. A ship detection method in SAR image based on Gravity Enhancement. *J. Remote Sens.* **2007**, *11*, 452–459. (In Chinese)
64. Kong, F. Maritime Traffic Monitoring and Analysis System Based on Satellite Remote Sensing. Master's Thesis, Dalian Maritime University, Dalian, China, 2009. (In Chinese).
65. Lecun, Y.; Bottou, L.; Bengio, Y.; Haffner, P. Gradient-based learning applied to document recognition. *Proc. IEEE* **1998**, *86*, 2278–2324. [CrossRef]
66. Ian, G.; Yoshua, B.; Aaron, C. *Deep Learning*; The MIT Press: Boston, MA, USA, 2016; pp. 326–366.
67. Nocedal, J. Updating quasi-newton matrices with limited storage. *Math. Comput.* **1980**, *35*, 773–782. [CrossRef]
68. Liu, D.C.; Nocedal, J. On the limited memory BFGS method for large scale optimization. *Math. Program. B* **1989**, *45*, 503–528. [CrossRef]
69. Davis, J.; Goadrich, M. The relationship between Precision-Recall and ROC curves. In Proceedings of the 23rd International Conference on Machine Learning, Pittsburgh, PA, USA, 25–29 June 2006; pp. 233–240.



© 2020 by the authors. Licensee MDPI, Basel, Switzerland. This article is an open access article distributed under the terms and conditions of the Creative Commons Attribution (CC BY) license (http://creativecommons.org/licenses/by/4.0/).